

See discussions, stats, and author profiles for this publication at: <https://www.researchgate.net/publication/238992121>

A study of wave propagation in varying cross-section waveguides by modal decomposition. Part II. Results

Article in The Journal of the Acoustical Society of America · May 1997

DOI: 10.1121/1.419306

CITATIONS

71

READS

502

3 authors:



Noam Amir

Tel Aviv University

111 PUBLICATIONS 2,870 CITATIONS

[SEE PROFILE](#)



Vincent Pagneux

French National Centre for Scientific Research

253 PUBLICATIONS 5,572 CITATIONS

[SEE PROFILE](#)



Jean Kergomard

French National Centre for Scientific Research

175 PUBLICATIONS 2,808 CITATIONS

[SEE PROFILE](#)

Some of the authors of this publication are also working on these related projects:



Voice and Emotions [View project](#)



PROPASYM : Acoustic asymmetric propagation based on nonlinear processes and time-dependent processes [View project](#)

A study of wave propagation in varying cross-section waveguides by modal decomposition. Part II. Results

N. Amir, V. Pagneux, and J. Kergomard

Laboratoire d'Acoustique de l' Université du Maine, URA 1101 CNRS, BP 535, Avenue Olivier Messiaen, 72017 Le Mans Cedex, France

(Received 25 March 1996; revised 13 December 1996; accepted 19 December 1996)

The full derivation of the equations governing the generalized impedance matrix Z , the pressure, and the velocity were presented in Part I of this series [Pagneux *et al.*, J. Acoust. Soc. Am. **100**, 2034–2048 (1996)]. Here only the results of that paper, i.e., the final set of equations which needed to be solved are repeated. Other factors influencing the solution are the boundary conditions at the end of the waveguide: Source and radiation conditions are also presented. Finally, the details of the numerical implementation are also relevant, and will be discussed in some detail. © 1997 Acoustical Society of America. [S0001-4966(97)02605-2]

PACS numbers: 43.20.Mv, 43.20.Ks, 43.75.Fg [JEG]

LIST OF SYMBOLS

z	axial coordinate
r	radial cylindrical coordinate
p	acoustic pressure
\mathbf{P}	column vector of coefficients of p for modal decomposition
\mathbf{v}	particle velocity
v_z	axial component of particle velocity
\mathbf{U}	column vector of coefficients of axial velocity for modal decomposition
c	speed of sound in free space
ω	angular frequency
k	wave number in free space
k_i	wave number of the i th mode in the waveguide
K	diagonal matrix of modal wave numbers; $K_{ij} = k_i^2 \delta_{ij}$

Z	generalized impedance matrix
Z_c	characteristic matrix impedance of a cylindrical pipe
Z_r	value of Z at the free end of the waveguide
Y	generalized admittance matrix
Y_r	value of Y at the free end of the waveguide
ψ	column vector of eigenfunctions in the waveguide
S	cross-sectional area of waveguide
R	local cross-sectional radius of waveguide
γ_i	i th zero of Bessel function J_1
A	diagonal matrix of γ_i/R
f	frequency
$\epsilon, \epsilon_r, \epsilon_v$	values used to calculate viscothermal losses
$D_i(\tau)$	function used to calculate radiation impedance
J_m	Bessel function of order m .

INTRODUCTION

This paper is the sequel to Part I,¹ where the theoretical background was presented. Here in Part II we will study in depth two typical waveguides. The first is a trombone bell, in which the flare increases very rapidly toward the end. We will calculate the input impedance and compare it to the measured input impedance, in order to show how the multimodal analysis improves on the results of plane-wave analysis. We will also examine the calculated pressure and velocity field along the horn. The second case is a waveguide with circular cross section, and an elliptic longitudinal section, in which we will study focalization effects and reflection properties. In both cases we show the effects of varying the parameters at our disposal on the solution, e.g., the number of modes taken into account, error thresholds, etc. As a matter of fact, the main goal of this part is the analysis of the field inside the guide with varying cross section, taking advantage of the specificity of the method. Incidentally, we compare the results with finite element results and experimental results, but this aspect is of secondary importance.

We will begin by reviewing in Sec. II the equations to

be solved numerically, followed by a description of the boundary conditions used for various types of radiation, and the numerical procedures used. Sections II and III then deal with the trombone horn and elliptic waveguide, respectively.

I. THEORETICAL BASIS

A. Equations

We wish to solve the matricial Riccati equation for the generalized impedance matrix Z :²

$$Z' = -j \frac{k\rho c}{S} + j \frac{S}{k\rho c} ZKZ + \frac{S'}{S} (QZ + ZQ). \quad (1)$$

Since Z is a matrix of infinite order, we must truncate it to order $n \times n$, where n must somehow be determined.

Once Z is known along the waveguide, we can find the pressure or axial velocity along the waveguide, integrating one of the two following equations:³

$$\mathbf{P}' = \frac{S'}{S} Q\mathbf{P} - j \frac{k\rho c}{S} \mathbf{U},$$

$$\mathbf{U}' = -j \frac{S}{k\rho c} \mathbf{K} \mathbf{P} - \frac{S'}{S} {}^t \mathbf{Q} \mathbf{U}. \quad (2)$$

Once P or U are found, the pressure or axial velocity are given by

$$p = \sum \psi_i P_i, \quad v_z = \frac{1}{S} \sum \psi_i U_i. \quad (3)$$

In certain cases it may be inconvenient to use the Riccati equation (1) for Z . If we define a generalized admittance matrix Y so that $U = YP$, we can obtain from (2) a Riccati equation for Y in the same way as (1) was obtained in Part I.¹ This equation will be

$$Y' = \frac{-jS}{k\rho c} \mathbf{K} - \frac{S'}{S} ({}^t \mathbf{Q} Y + Y \mathbf{Q}) + \frac{jk\rho c}{S} Y Y. \quad (4)$$

A further refinement to these equations is the introduction of viscothermal losses created at the boundaries. Keeping in mind that the expression K is simply a diagonal matrix of propagation constants for the various modes, we can simply replace it in Eqs. (1) and (4) by an expression for the lossy propagation factors. This can be found in Ref. 4. For the axisymmetric modes it is as follows:

$$k_i^2 \approx k^2 - \left(\frac{\gamma_i}{R} \right)^2 + 2k[\text{Im}(\epsilon_i) - j \text{Re}(\epsilon_i)]. \quad (5)$$

At atmospheric pressure and room temperature, ϵ_i can be approximated as

$$\epsilon_i = \left(1 - \frac{\gamma_i^2}{R^2 k^2} \right) \epsilon_v + \epsilon_t, \quad (6)$$

where $\text{Re}(\epsilon_v) = \text{Im}(\epsilon_v) = 2.03 \times 10^{-5} f^{1/2}$, and $\text{Re}(\epsilon_t) = \text{Im}(\epsilon_t) = 0.95 \times 10^{-5} f^{1/2}$ (f in s^{-1}).

B. Boundary conditions

The general problem we aim to solve in this paper is as follows: Given a rigid walled waveguide, we have a source at one end, and a radiating termination at the other. The source can be a pressure or velocity source, thus fixing either P or U at one end. The radiation condition must fix the value of the matrix Z at the other end, which we will call Z_r .

One simple case is a termination consisting of an infinite cylindrical tube. In this case, Z_r is simply a diagonal matrix of characteristic impedances for each mode and $Z_r = Z_c$. Another simple case is the “ideal reflection” of an open end; i.e., each mode has a pressure node at the open end, and thus Z_r is uniformly zero. Such a boundary condition for the impedance matrix is a very rough approximation of an open end. Even in the plane-wave approximation, a length correction has to be taken into account. On the other hand, if we wish to model a closed end, the axial velocity is zero, thus elements of Z_r need to be infinite. In this case it is easier to solve the equation for Y , Eq. (4), with a uniformly zero boundary condition for Y_r . The value of Z at the input can be obtained by inverting Y .

The most complicated case is the most realistic one, of radiation into free space. This is quite difficult to solve, therefore we chose to adopt instead the radiation into a half-

space; the open end of the waveguide is thus placed in an infinite baffle. This case has been treated before in Refs. 5 and 6. Initially, the analytical expression for Z_r is

$$Z_r = \frac{j\omega\rho}{S^2} \int_S \int_S \psi(\mathbf{w}) G(\mathbf{w}, \mathbf{w}') {}^t \psi(\mathbf{w}') ds dS', \quad (7)$$

where $G(\mathbf{w}, \mathbf{w}')$ is the Green's function for radiation into the half-space, and \mathbf{w} is a vector on S . This integral is singular and thus difficult to evaluate directly. Therefore we chose to use the formulation presented by Zorumski,⁵ which seems to be posed most efficiently for numerical evaluation. The expression for Z_r presented by the latter are

$$Z_{ij} = -j \int_0^\infty \tau (\tau^2 - 1)^{-1/2} D_i(\tau) D_j(\tau) d\tau. \quad (8)$$

Here, Z_{ij} is a nondimensional form of Z_r and D_i is defined by

$$D_i(\tau) = k^2 \int_0^r r J_0(\tau k r) \psi_i(r) dr. \quad (9)$$

Zorumski provides an exact analytical solution for (9), and another form of (8) which can be numerically evaluated more readily:

$$Z_{ij} = \int_0^{1/2\pi} \sin \phi D_i(\sin \phi) D_j(\sin \phi) d\phi - j \int_0^\infty \cosh \xi D_i(\cosh \xi) D_j(\cosh \xi) d\xi. \quad (10)$$

These results were compared to another calculation based on Ref. 6, giving very good agreement.

Since this expression for the radiation impedance is the closest available to us, we compared the theoretical results to experiments both with and without an “infinite” baffle, in order to have an idea of how far this radiation condition is from radiation with no baffle. An extension of the calculation of the case with infinite baffle to the case of no baffle could be made by iterative procedure (see Williams⁷).

C. Numerical procedures

The basic “engine” used to solve the Riccati equations for Z or Y was a third- or fourth-order Runge–Kutta procedure. This proved to be relatively robust in most cases. Divergence did occur when using simplified radiating conditions where no energy was allowed to radiate from the waveguides (the closed or “ideal open” terminating conditions), since the impedance or admittance peaks became infinite. In these cases it was imperative to incorporate boundary layer thermal and viscous losses into the calculation, as described above.

It is also imperative to use an adaptive stepsize, even with radiation or viscous losses, since the peaks in Z or Y can be pronouncedly sharp, and there is no way to predict the necessary minimum stepsize. This type of solution requires selection of an error threshold for determining when the stepsize must be reduced; this threshold must be selected by trial and error. If it is not small enough, the computation will generally diverge. It may noticed that the effect of increasing

the number of modes selected reduces the Runge–Kutta stepsize, because with more modes we have more peaks for the impedance.

Once Z or Y have been integrated from the radiating end to the source, it remains to calculate the pressure or velocity field, integrating one of (2) in the other direction, i.e., from the source to the radiating end. This requires knowledge of Z or Y at each point of integration. This is a touchy point: As described in Part I, an attempt to reintegrate either of these values back up the waveguide always fails. This means that Z or Y must be stored at each point during the numerical solution of the Riccati equations, to be used later when integrating for \mathbf{P} or \mathbf{U} . This creates two problems: It can take up much memory, and it fixes the integration points for their computation. The first problem has no easy remedy—the RAM memory at the program’s disposal must be sufficiently large, or disk space should be used (slowing down the calculation considerably). The second problem means that an adaptive stepsize cannot be used for the second integration.

In practice, Z was stored during the first integration on a grid of regularly spaced points along the axis, by “forcing” the adaptive stepsize algorithm to “visit” these points in addition to any intermediate points required by the algorithm. The second calculation was then performed with a fixed stepsize. As a coherence check, the energy flux was calculated along the waveguide, using lossless propagation. When it came out nearly constant (relative error of less than 0.1%) the calculation was judged to be sufficiently accurate. This procedure necessitates a very fine grid for storing Z , although apparently this is the only method possible.

We will demonstrate in the later sections how various choices of parameters influence the results of the computation.

II. FIRST WAVEGUIDE: THE TROMBONE BELL

The first case to be studied in detail is the trombone bell, which comprises approximately the last 55 cm of the instrument. It is characterized by a rapid flare at the end, which should render one-dimensional analysis methods relatively inaccurate. In this section we will study the theoretically computed input impedance and compare it to results obtained experimentally. We will also examine the pressure field inside the horn.

The objective of this study is not only to verify the theoretical results by comparison to experiments, but also to study the influence of various parameters on the theoretical results. We wish to see the influence of various radiation conditions, the effect of the number of modes used on the accuracy, and the interaction between these parameters. Another point to be examined is how the assumption of an infinite baffle can change the experimentally measured input impedance.

We will begin with a description of the geometry of the horn, and its relation to the frequency range considered. This will be followed by a short description of the experimental apparatus, and then by comparisons of theoretically and experimentally obtained input impedances. The final part of the section will present results concerning the pressure field.

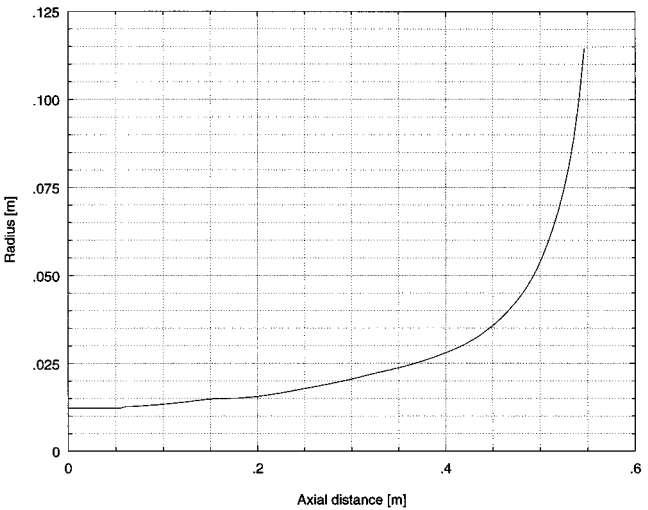


FIG. 1. Radius of the trombone horn versus axial distance.

A. Geometry and frequency

The part of trombone studied begins with a cylindrical section of 25.4-mm diameter. It then begins to flare modestly, terminating in an abrupt flare to $R=115.4$ mm The radius as a function of distance appears in Fig. 1. Table I summarizes the points that were measured. Intermediate points were obtained by third order polynomial interpolation; a polynomial was calculated for four points at a time, and used for calculating values between the two middle points only.

The frequency range to be studied was between 0 and 1200 Hz, this being approximately the musically useful range of the trombone. It is interesting to note that for this range of frequencies, all of the higher order modes are in cutoff, even at the mouth of the horn. At the throat of the horn this is 7.2% of the first cutoff frequency, and at the mouth it is 65% of the first cutoff frequency. The excitation is assumed to be a plane piston, i.e., only the plane-wave mode is excited at the throat, and any influence of higher order modes is due to mode coupling induced by the flare. These higher-order modes are assumed to be so deeply in cutoff at the throat that they can be ignored there, therefore enabling us to treat the input impedance as a simple scalar value, which is the corner value of the matrix Z . The validity of this assumption will be examined later.

B. Experimental apparatus and results

The experimental apparatus available enabled us to measure the input impedance of the horn, but not the pressure field. This apparatus consisted of a velocity source and a

TABLE I. Radius of the trombone horn versus axial distance.

distance [cm]	0	5.5	5.6	5.7	5.8	5.9	8.3	12.4
radius [cm]	12.25	12.25	12.25	12.25	12.65	12.65	13	14
distance [cm]	16.2	20.3	25.3	31.2	36	40	43.2	45.7
radius [cm]	15	16.5	18.5	21.5	24.5	28	32	37
distance [cm]	48.2	50	51.5	52.7	53.6	54.4		
radius [cm]	44.5	52	62	74.5	89.5	114.5		

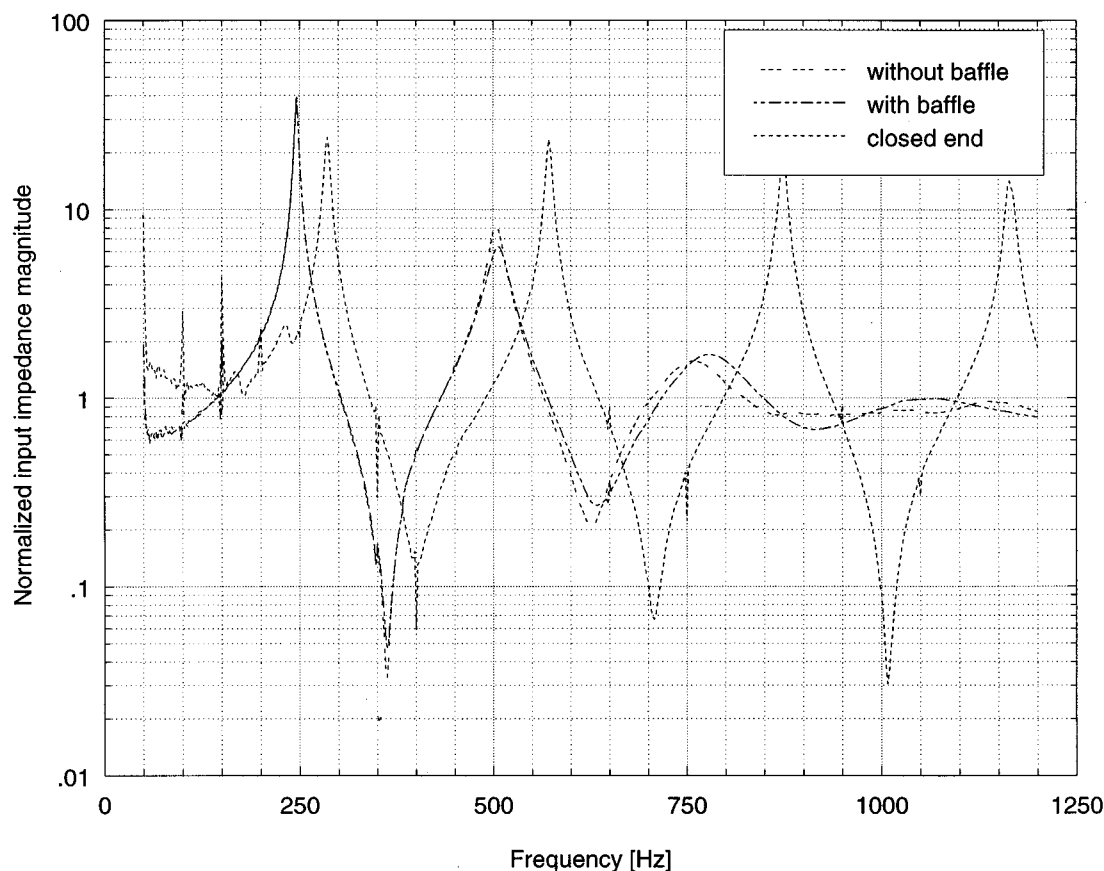


FIG. 2. Measured input impedance with baffle, without baffle, and with rigid sealed end. Note the difference between the first two, at high frequencies.

pressure sensitive microphone at the throat of the horn, both connected to a lock-in amplifier. The latter is connected to a PC, which controls the frequency sweep. This sweep is performed adaptively, so that smaller increments are taken near the impedance peaks, ensuring good accuracy in these regions. The entire apparatus was placed in an anechoic chamber, and performed at a controlled temperature. Calibration was carried out using a cylindrical pipe of approximately 1 m length. For further details of this apparatus, refer to Ref. 8.

The measurements were carried out for three cases: one where the horn radiated freely into the room, one where the mouth was placed in a large baffle (1.5×1.5 m), and one where the end of the horn was shut hermetically with a flat Plexiglass plate.

Figure 2 shows the results of these three measurements. Note that there is a subtle but noticeable difference between measurements made with and without the baffle, at higher frequencies. This is important, since the theoretical calculations use the baffled value of the radiation impedance. This is also used often in the literature for the one-dimensional models, although without always specifying whether the experiments used a baffle also. Fortunately, at low frequencies the two measurements give practically identical results; at such frequencies a good approximation of an infinite baffle would have to be very large. At frequencies where the two measurements differ, the baffle used was in fact a good approximation of an infinite one. The reasons for this behavior are explained in Ref. 9, where it is shown that musical horns are

quite insensitive to the radiation impedance at low frequencies, and that even plane-wave calculations can give good results at these frequencies.

Figure 2 also shows a big difference between measurements with an open and closed horn. The closed horn has no radiation losses, and being quite short the viscothermal losses are quite small also, therefore the impedance peaks are similar in height, and at different frequencies than those found for the open horn.

C. Theoretical results for input impedance

Before comparing the theoretical and experimental results, we examine the purely theoretical results from several points of view.

As stated above, the parameter we will be dealing with will simply be the corner value Z_{00} of the matrix Z . Before continuing, the assumption that this parameter is the main one of importance must be justified. In Fig. 3 we show the diagonal of Z as a function of frequency, and the first row of Z as a function of frequency. These represent, respectively, the “self” impedances of each mode, and the “cross” impedance between the higher-order modes and the plane-wave mode. The very low values of all the other elements in relation to the corner value shows that their importance is minimal. They are also generally quite smooth, as opposed to the peaks and dips found in Z_{00} , thus giving no information concerning resonances or antiresonances.

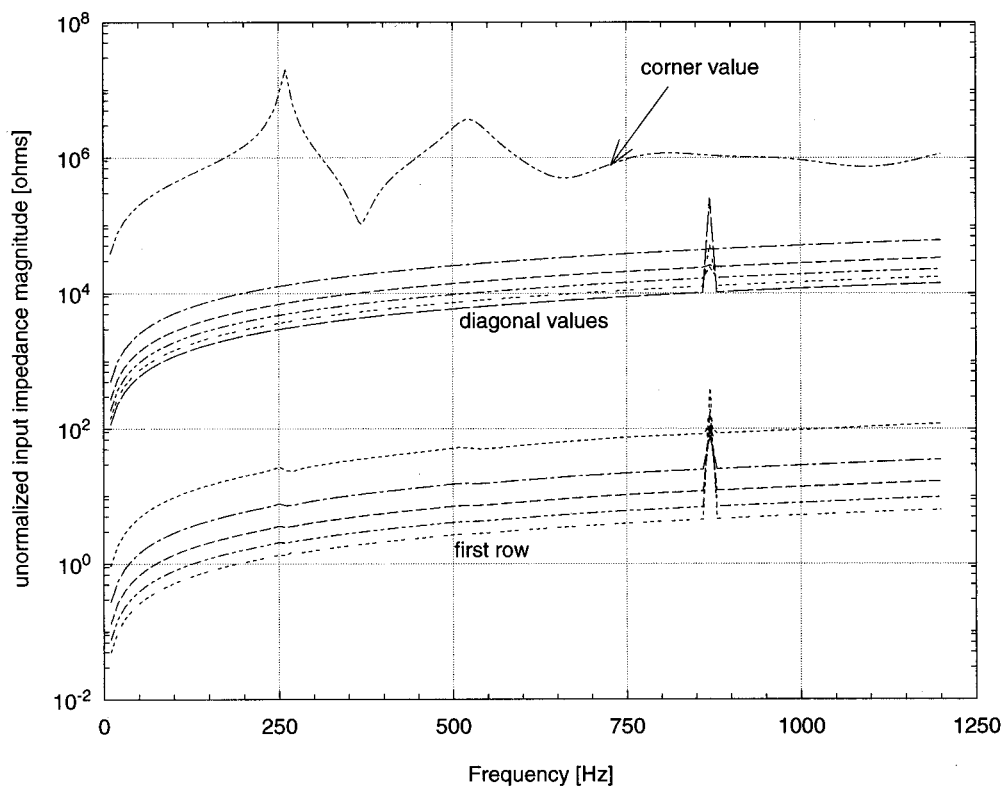


FIG. 3. The diagonal and first row of the input impedance matrix Z (arbitrary units).

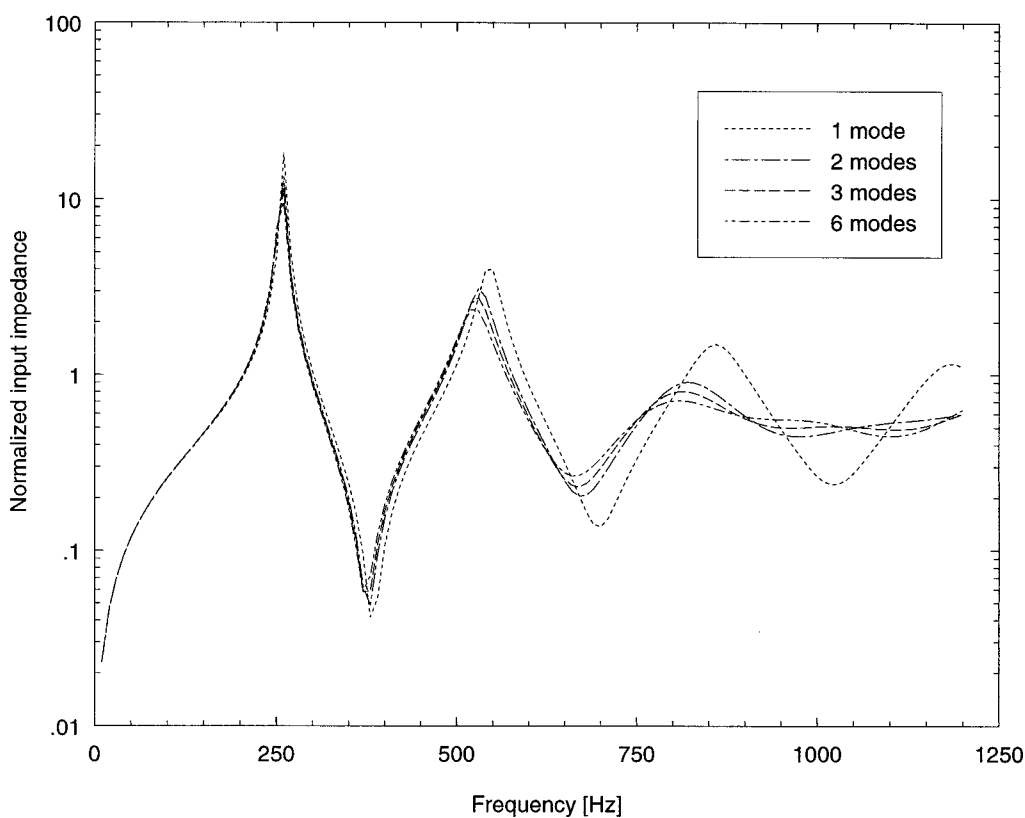


FIG. 4. The corner value of Z calculated with progressively more modes. One mode=plane-wave mode only.

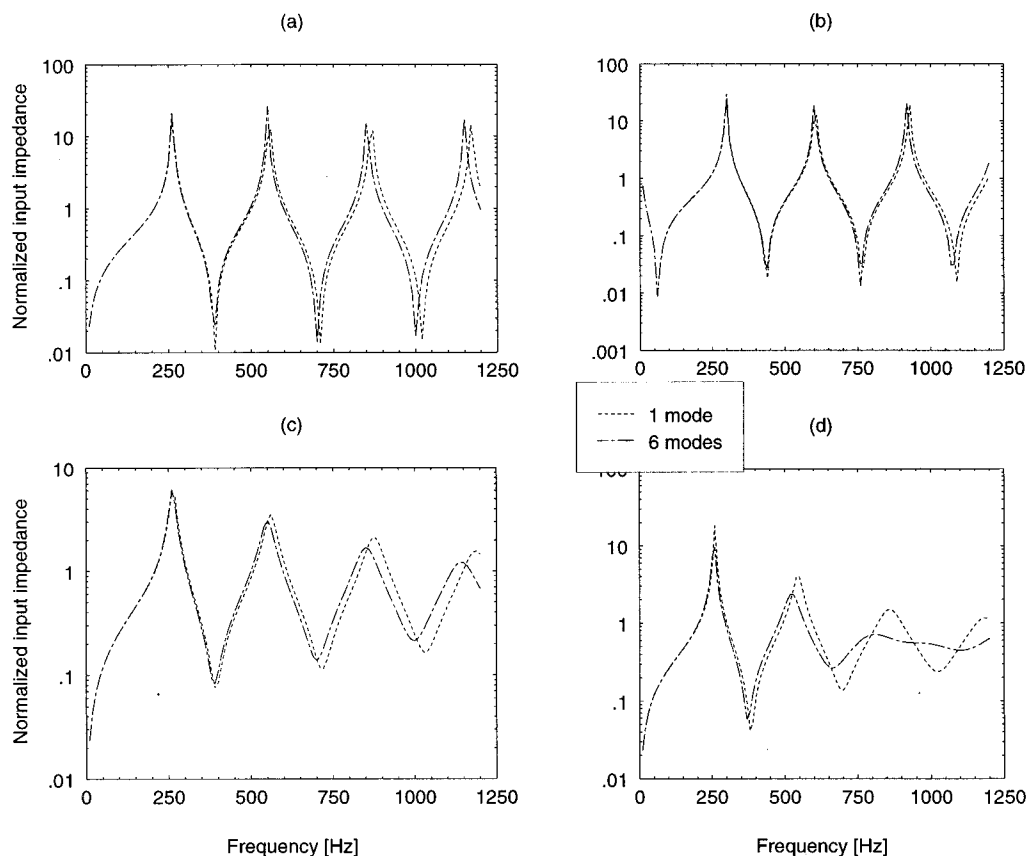


FIG. 5. Comparison of input impedance calculated with plane-wave mode and with six modes for four different end conditions: (a) closed end; (b) ideal open end; (c) infinite pipe termination; and (d) baffled radiation model. Note that the largest difference between the two calculations is found in (d).

An interesting artifact found in the other elements of Z is the appearance of spurious peaks. These are simply artifacts of the numerical calculation, and can be made to disappear if a smaller stepsize is constrained, by using a smaller error threshold in the Runge–Kutta algorithm. This lengthens the calculation time, with very little effect on the resulting value of Z_{00} . Therefore, to a certain extent these artifacts were allowed. It is the adaptive stepsize which “returns” the diverging curves to their normal values; using a fixed stepsize allowed these artifacts to cause the whole algorithm to diverge.

The most important parameter of the calculation is the number of modes used, i.e., the order to which the matrix Z is truncated. In Fig. 4 we show the corner value computed with different sizes of Z . The most radical change occurs when adding just one mode to the basic plane-wave model. Afterward the differences are small, becoming progressively smaller, and more obvious at higher frequencies. For our calculations we generally used six modes, even though all the higher order modes were evanescent. In general, this parameter strongly depends on the frequency range being studied, and on the irregularity of the horn walls.

It is of primary interest to view how much the introduction of the higher-order modes changes the results, as compared to plane-wave analysis, or spherical wave analysis. In this context we studied a number of possible radiation impedances: the hole-in-infinite-baffle, zero radiation impedance (“ideal open end”), infinite impedance (closed end),

and termination by an infinite cylindrical pipe. Not all of these, of course, could be implemented experimentally.

In Fig. 5 we see for each of these a comparison of the input impedance calculated with one and six modes. In all cases there is good agreement at low frequency, less so at higher frequency. The difference is most marked for the most practical case of radiation into a baffled space. For a closed horn, on the other hand, we can expect good results even with a plane-wave model, as has already been shown in Ref. 9.

Another interesting point is to compare the input impedances calculated with different boundary conditions. This is carried out in Fig. 6 for 1 and 6 mode calculations. As also shown in Ref. 9, the resonance frequencies for all cases except for the closed end are very near each other for the plane-wave calculation. This quality of musical horns is actually an artifact of the plane wave model, as shown by experiments in Ref. 9, and borne out by the six mode calculation shown here; at low frequencies it remains true, but at higher frequencies the peaks for the baffled radiation case are very low, and at very different frequencies than the others.

D. Comparing theory and experiments

The most important comparison carried out here is that of the multimode calculation with the experimental results. This appears for theoretical and experimental results in Fig. 7. A good agreement is observed, better than the result ob-

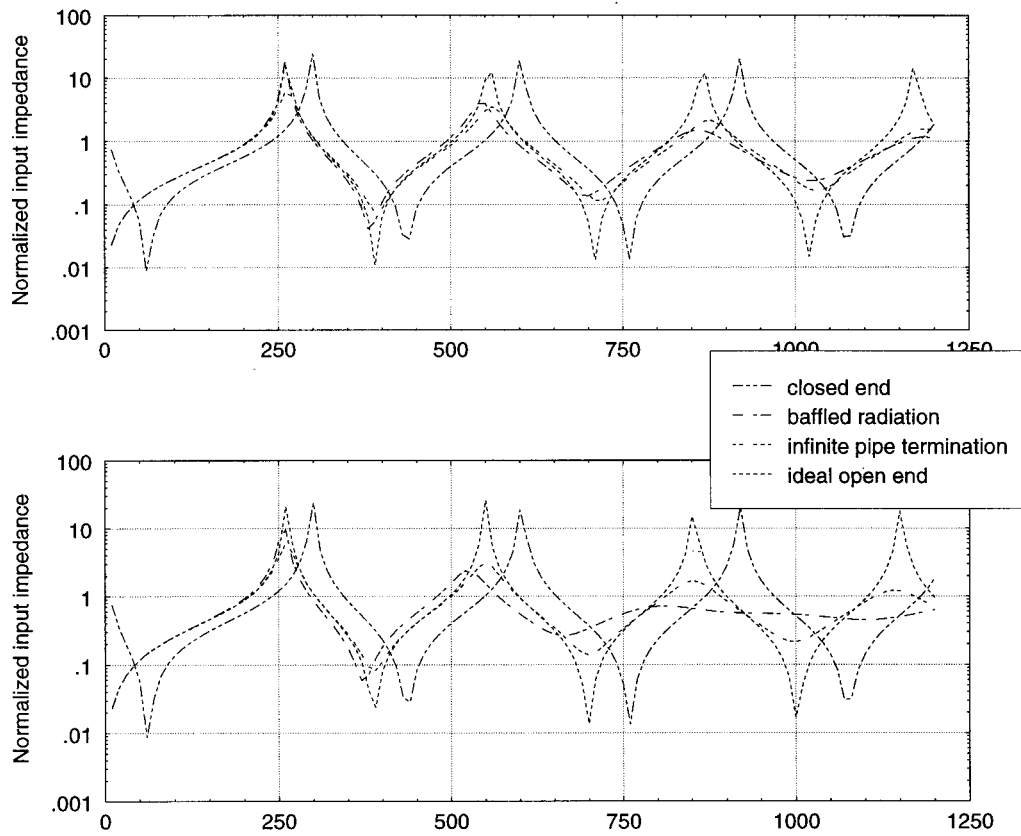


FIG. 6. Comparison of input impedances for four end conditions: (a) with plane-wave mode only; (b) with six modes.

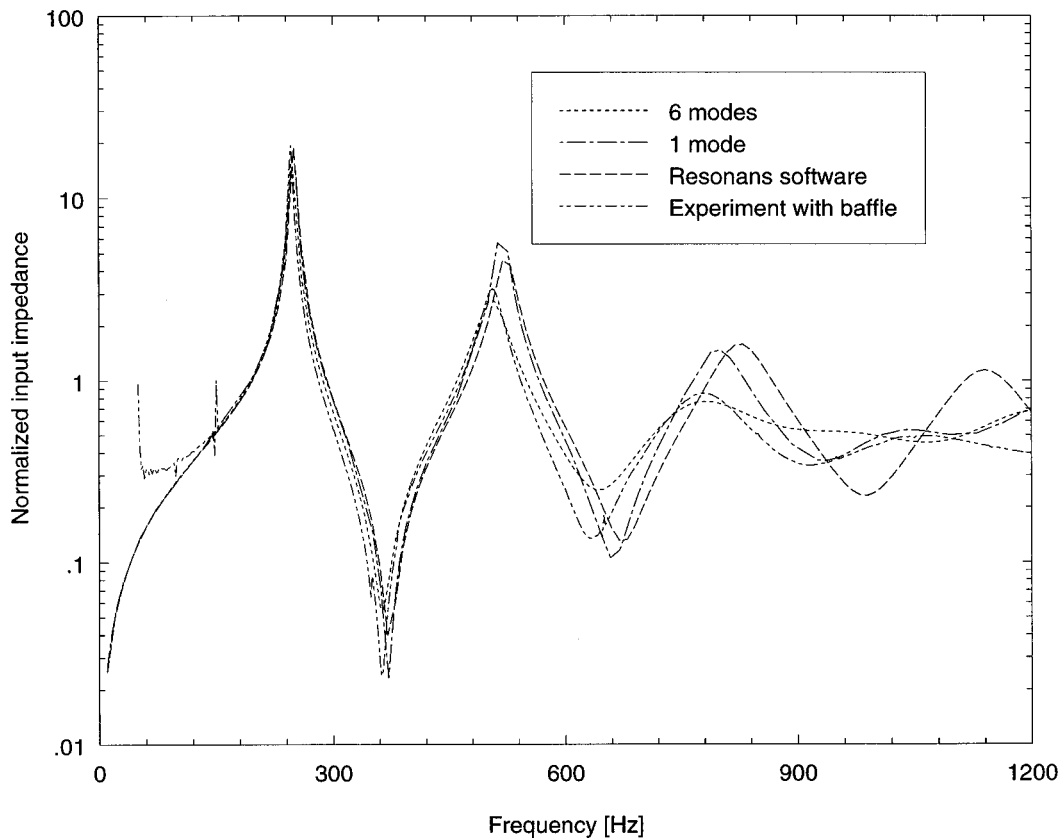


FIG. 7. Comparison of experimental input impedance with various theoretical curves. Best agreement is achieved with the multimodal calculation.

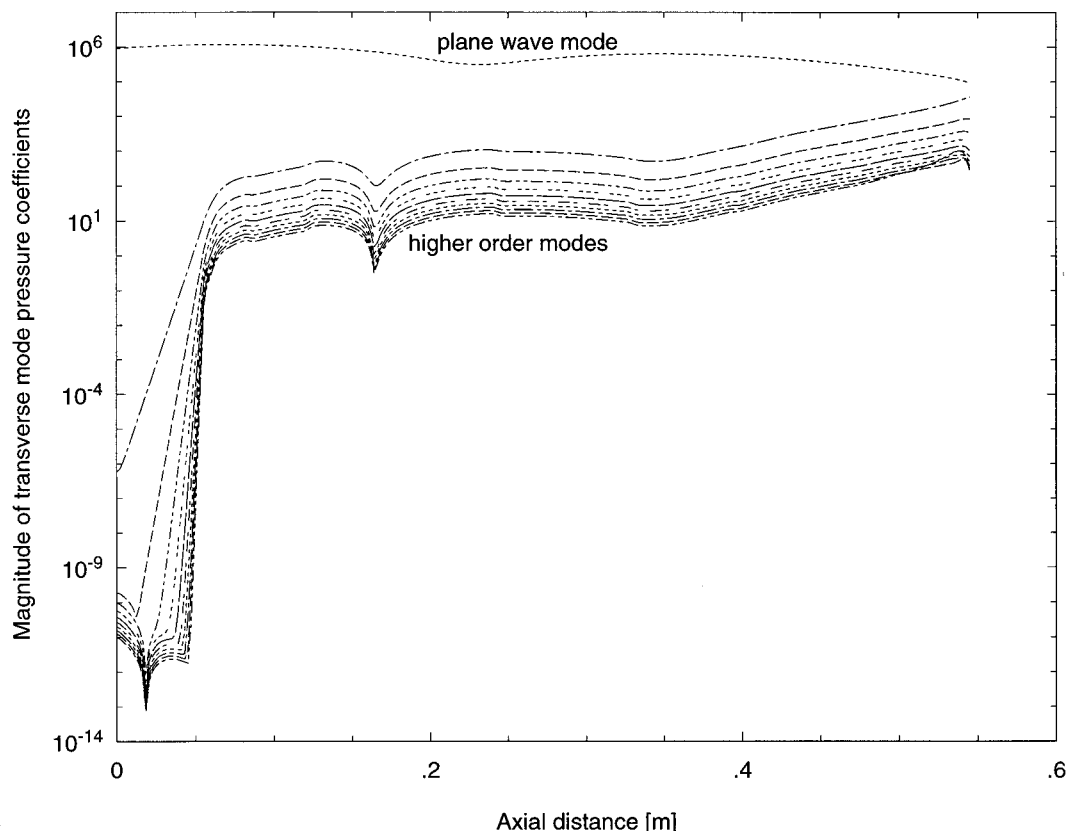


FIG. 8. Coefficients of the pressure series expansion along the horn. Note that the higher-order modes are significant only near the mouth of the horn.

tained using only the lowest order mode. The validity of the simplest model, with only the plane-wave mode, is confirmed for the trombone to be limited to roughly 500 Hz, as predicted, using simple arguments, by Kergomard.¹⁰ On the other hand we do not obtain perfect agreement, unfortunately. A further study is necessary in order to verify the source of this error.

E. Calculations of the pressure and velocity fields

In this section we present calculations of the pressure and velocity fields along the horn for various frequencies, usually with a plane piston (velocity source) excitation.

Our first example is a plane piston excitation at 600 Hz using 11 modes. In Fig. 8 we see the values of the coefficients \mathbf{P} along the horn. From this figure it is clear that the higher-order modes modify the pressure field only toward the very end of the horn, where the flare is largest. This justifies once more the use of a scalar input impedance at the throat.

Next, in Fig. 9 we show graphs of equipressure surfaces toward the end of the horn, using 2, 6, and 11 modes. Despite the small coefficients in \mathbf{P} for the higher order modes, the differences between the figures are clearly visible. Obviously, to obtain a good visual representation of these surfaces, a relatively large number of modes must be used, even though they are all evanescent.

Raising the frequency can create a much more complicated picture. In Fig. 10 all of the higher order modes are

evanescent. At this frequency the equipressure surfaces are far from being spherical.

One more comparison we made is the axial pressure calculated by modal analysis to the axial pressure obtained with the horn equation, i.e., using only the plane-wave mode. This appears in Fig. 11. A considerable difference is apparent.

III. SECOND WAVEGUIDE: THE ELLIPSOIDAL INDENTATION

In this section we show how the method can be applied to a cylindrical duct with an ellipsoidal indentation. The geometry, which is axisymmetric, is characterized by the radius of the cylindrical duct R_0 , the maximum radius of the indentation R_{\max} , and by the distance between the two focal points L (see Fig. 12).

Our first objective is to observe how the transition from low frequencies to higher frequencies is accompanied by an increase of the focalization at the right focal point M_f . This guide is excited by a monopole located at the left focal point M_0 . Classical analysis of the radiation of monopole source into a straight waveguide can be found in classical works (see Morse and Ingard¹¹ and Doak¹²). The influence of the number of modes selected is also analyzed and comparisons with a finite element method (FEM) code (ANSYS) are made.

In a second part, in the same geometry, the Riccati equation (1) is integrated to find reflection properties of the geometry with two different maximum radius of the indentation, R_{\max} .

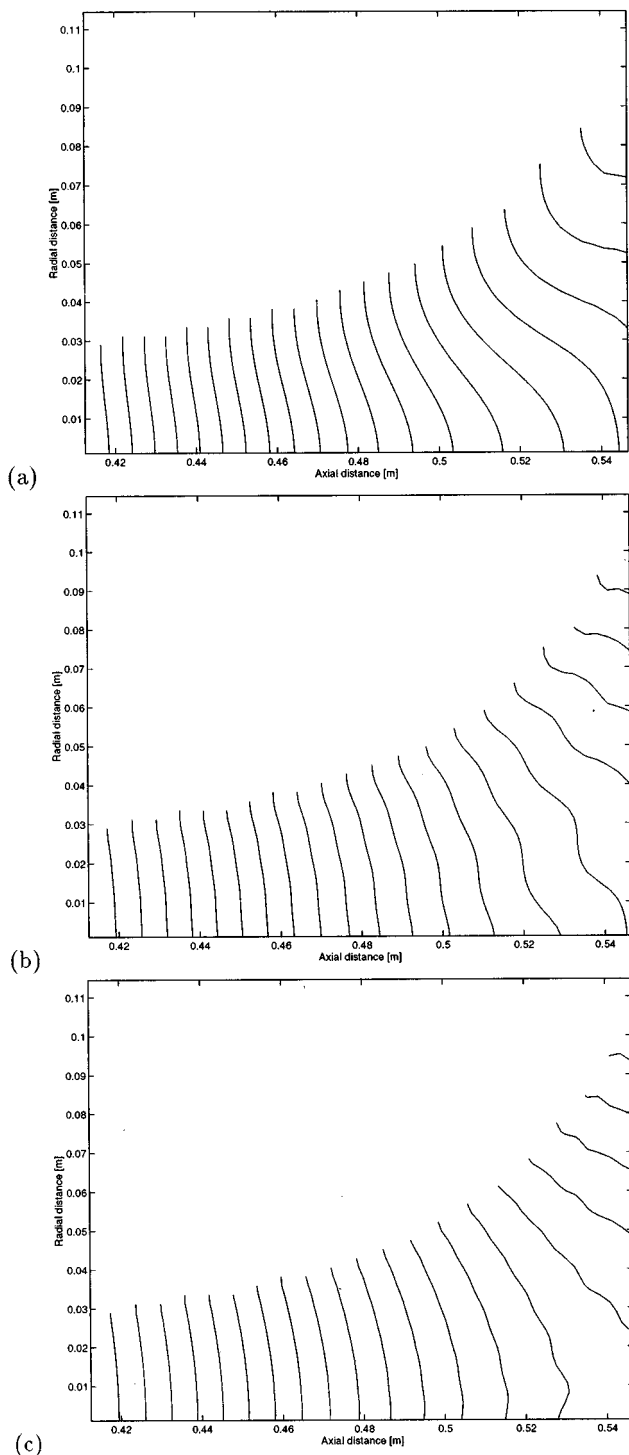


FIG. 9. Equipressure surfaces along the last 14 cm of the horn, at 600 Hz, calculated with: (a) 2 modes; (b) 6 modes; (c) 11 modes.

A. Study of the focalization

1. Procedure

According to the reasoning of geometrical acoustics, if a signal is launched from the left focal point M_0 , a receiver located at the right focal point M_f will observe a focalization. This is due to the fact that each ray emitted from M_0 has to go to M_f with the same phase shift. This is true in a complete ellipsoidal geometry and under the assumption of

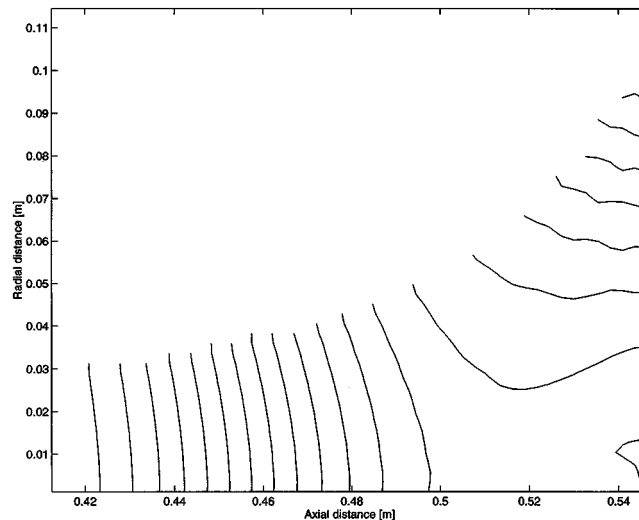


FIG. 10. Equipressure surfaces along the last 14 cm of the horn, at 1200 Hz, calculated with 11 modes.

very high frequency. Here the effects may be modified due to truncation of the ellipsoidal geometry and to finite wavelengths.

Three different frequencies have been selected for the analysis. In the first case, where $kR_0 = 1.85$, only one mode is propagating, therefore it is possible to compare with the classical MPWA (matched plane-wave approximation) calculation and to observe the advantage of a multimodal approach even at low frequency. In the second case, where $kR_0 = 7.4$, three modes are propagating. In the third case, where $kR_0 = 14.8$, five modes are propagating in the cylindrical duct. The peculiar interest here is that a sixth mode can propagate in the indentation only, making this mode a localized one. We can therefore examine whether our method is still efficient in such a case.

Boundary conditions at the right and at the left end of the guide are those of infinite propagation without reflection, i.e., $Z = Z_c$ (resp. $Z = -Z_c$) at the right (resp. left) termination. Calculations were made using the following procedure; first, starting from the right boundary condition ($Z = Z_c$), the

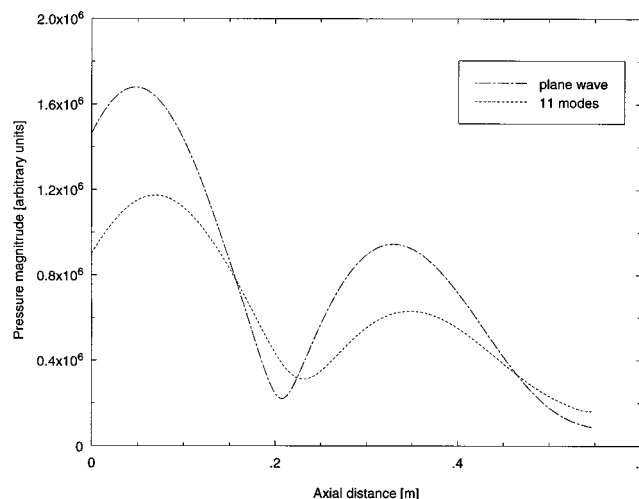


FIG. 11. Pressure amplitude along the axis of the horn, at 600 Hz, calculated with 1 and 11 modes.

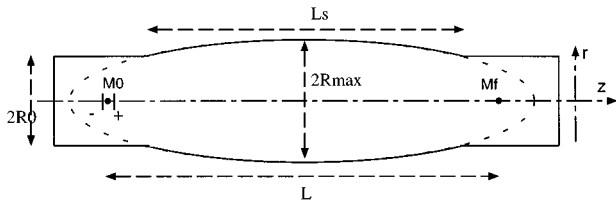


FIG. 12. Geometry with ellipsoidal indentation. The two points, M_0 and M_f , are focal points located at positions $\pm 1.2R_0$.

Riccati equation is integrated down to the point M_0 . Then we have $P_0^+ = ZU_0^+$ valid at the right of M_0 , where + and – will be thereafter related to quantities at the right and left limit of M_0 . On the other hand, knowing that the left termination is infinite, we have $P_0^- = -Z_c U_0^-$ valid at the left of M_0 . Finally, it is possible to get the velocity coefficients of the source by applying the conservation of pressure and flowrate,

$$P_0^+ - P_0^- = 0$$

and

$$U_0^+ - U_0^- = Q,$$

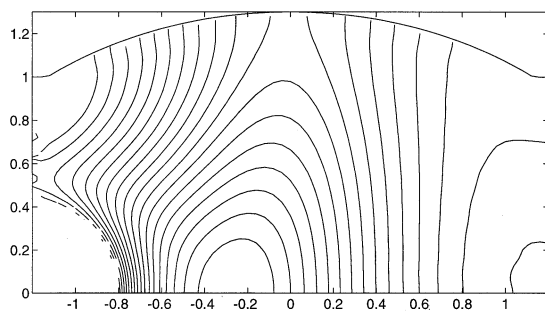
where vector Q contains the coefficient $Q_j = q_0 \psi_j(0)$ of the projection of the monopole of strength q_0 (flowrate source) on the function ψ_m . This gives us

$$U_0^+ = (Z_c + Z)^{-1} Z_c Q.$$

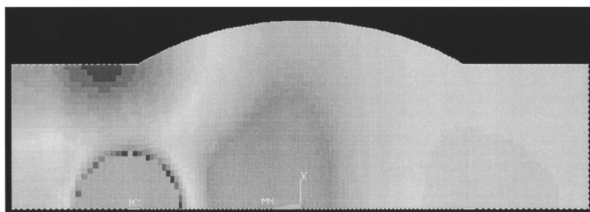
Finally, Eq. (2) is integrated to yield the field across the waveguide.

2. Frequency below the first cutoff of the waveguide

Figure 13 shows the modulus of the pressure for such a low frequency. Our method [Fig. 13(a)] achieves very good agreement with the pattern obtained from the FEM code

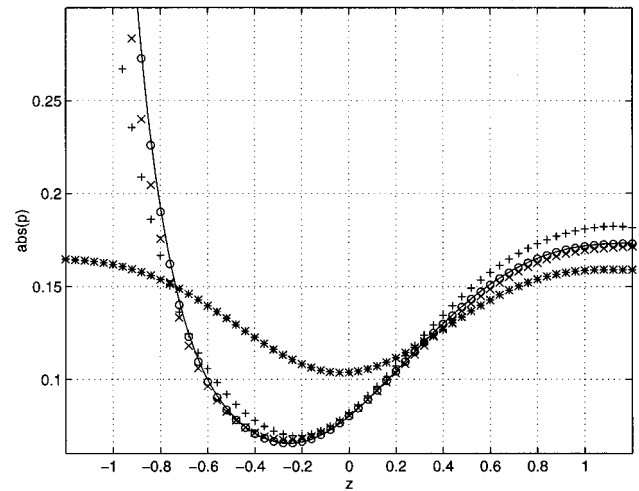


(a) multimodal

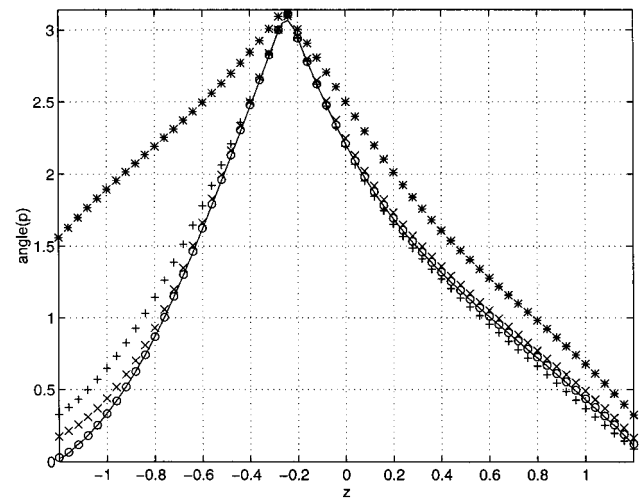


(b) FEM code

FIG. 13. Modulus of the pressure, $kR_0 = 1.85$.



(a) modulus of the pressure



(b) phase of the pressure

FIG. 14. Modulus and phase of the pressure along the central line $r=0$, $kR_0 = 1.85$. (*): 1 mode; (+): 2 modes; (×): 3 modes; (○): 15 modes; plain line: FEM method.

[Fig. 13(b)]. In the two figures, a light focalization can be observed even at this rather low frequency. In order to quantitatively compare the two computations, we have plotted the profiles of the modulus and of the phase of the pressure along the central line ($r=0$) in Fig. 14; four different calculations with different numbers of modes ($m=1, 2, 3$, and 15, where m is the number of modes) are compared to the FEM profile. It is very clear that selecting only one mode ($m=1$, corresponding to the MPWA method) is not sufficient to yield the correct result. Adding just one mode to the modeling ($m=2$) enables to improve the agreement. Eventually, with 15 modes ($m=15$) the agreement between the multimodal and the FEM approaches is almost perfect.

Another view of the effect of the multimodal convergence is seen in Fig. 15, where the pattern of the modulus of the pressure is plotted for 1, 2, 3, and 15 modes. This shows the failure of the MPWA method ($m=1$), but as soon as two modes are used, a roughly correct pattern is obtained. As

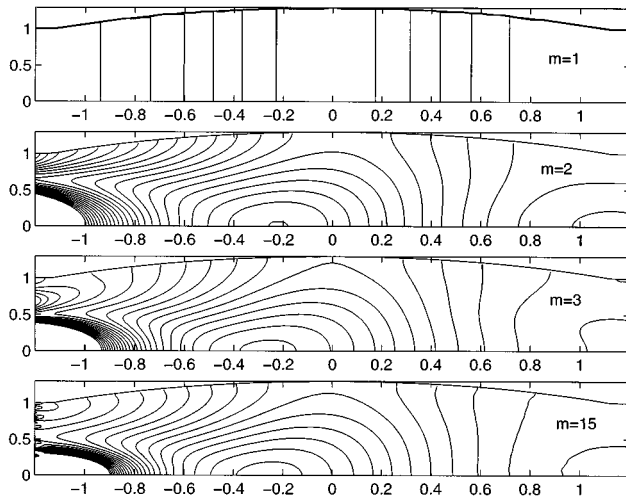


FIG. 15. Modulus of the pressure with 1, 2, 3, and 15 modes, respectively.

m is increased, the pressure tends to achieve the boundary condition at the wall ($\partial p / \partial n = 0$), due to the increasing number of evanescent modes used.

We also measured the rate of convergence of the multimodal method in Fig. 16. The result obtained with 15 modes is chosen as the reference, and three different quantities are proposed for the error ϵ :

$$\epsilon_1 = \frac{\int_V \|p - p_{\text{ref}}\|^2 2\pi r dr dz}{\int_V \|p_{\text{ref}}\|^2 2\pi r dr dz},$$

$$\epsilon_2 = \frac{\int_V \|p - p_{\text{ref}}\|^2 dr}{\int_V \|p_{\text{ref}}\|^2 dr},$$

$$\epsilon_3 = \frac{\int_{r=0} \|p - p_{\text{ref}}\|^2 dz}{\int_{r=0} \|p_{\text{ref}}\|^2 dz}.$$

Here, ϵ_1 represents the actual error in the volume, ϵ_2 is the error ignoring the axisymmetry of the geometry, and thus stressing the difference along the central line ($r=0$), ϵ_3 is the error only along the central line.

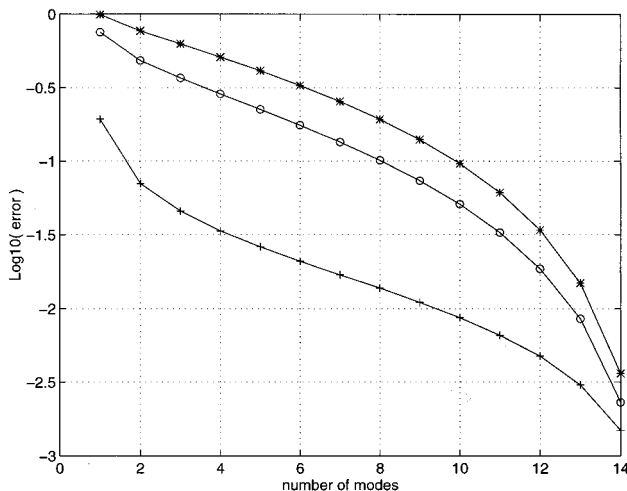
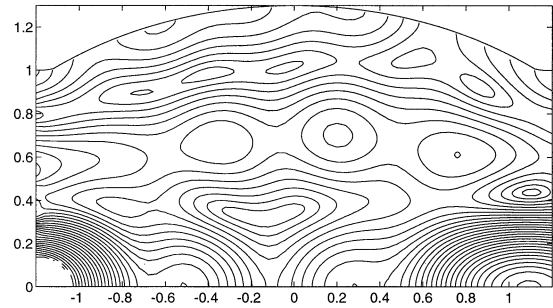
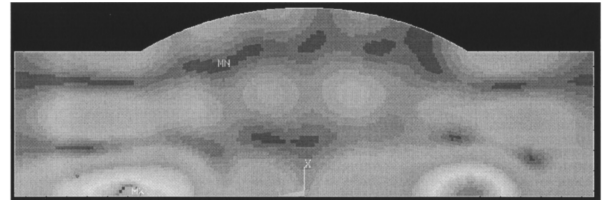


FIG. 16. Error of the method. (+): ϵ_1 , (O): ϵ_2 , (*): ϵ_3 .



(a) multimodal



(b) FEM code

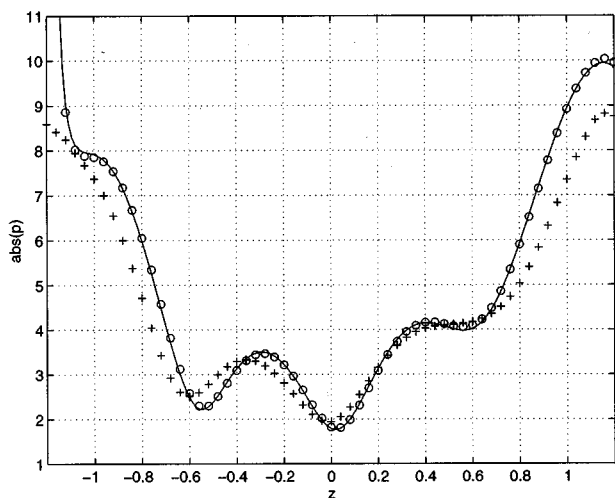
FIG. 17. Modulus of the pressure, $kR_0 = 7.85$.

Figure 16 shows that all three error measures decrease monotonically as more modes are introduced in the calculation. The increased values of ϵ_1 , ϵ_2 , and ϵ_3 , respectively, are due to the fact that the source is a monopole located on the central line; ϵ_1 , ϵ_2 , and ϵ_3 take this progressively more into account.

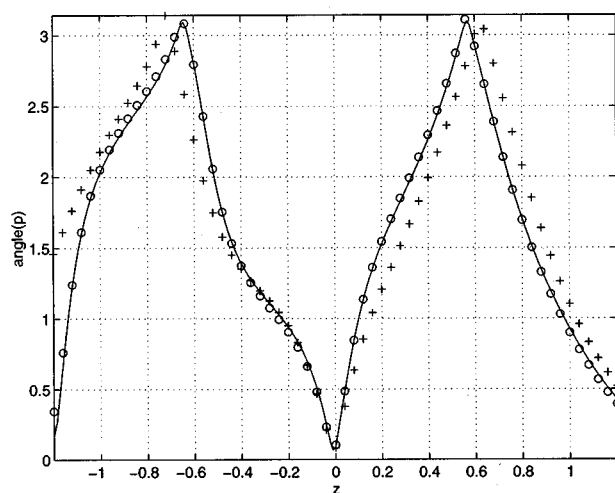
The behavior of ϵ_1 is almost exponential, except between $m=1$ and $m=2$ where the error is reduced. That shows, once more, that even with only two modes a large degree of accuracy is gained with the multimodal method.

3. Higher frequencies

When the frequency is increased to $kR_0 = 7.85$, three modes are propagating and the focalization increases as can be seen in Fig. 17. Figure 17(a) and (b) show the agreement between the multimodal and the FEM computations, as far as the pattern is concerned. On the other hand, when the profile of the modulus of the pressure along the central line ($r=0$) is plotted, we discover some discrepancies. In fact, the latter are an artifact of the FEM code since it is unable to model the correct infinite termination condition at the extremities of the guide. We therefore repeated the comparison (Fig. 18), but this time applying in the multimodal calculation the same condition as in the FEM code ($p = \rho_0 c u_z$) at the extremities ($z = \pm 2R_0$). This is equivalent to imposing $Z_{nm} = \delta_{nm} \rho_0 c / S$ for the matrix impedance, rather than the correct infinite termination condition which is $Z_{nm} = Z_{cnm} = \delta_{nm} \rho_0 c k / (S k_n)$. The three profiles corresponding to the correct and incorrect termination conditions and to the FEM code are plotted in Fig. 18. We see that incorporating the same boundary condition as the FEM code in our multimodal method enables us to obtain an excellent agreement. Nevertheless, one has to keep in mind that the actual correct solution is the multimodal one with correct boundary condition. Obviously this difficulty of the FEM could be overcome by



(a) modulus of the pressure



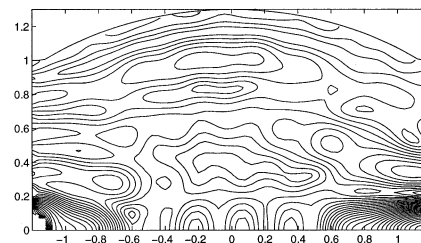
(b) phase of the pressure

FIG. 18. Modulus and phase of the pressure along the central line $r=0$, $kR_0=7.85$. (+): correct boundary condition; (O): incorrect boundary condition; plain line: FEM method.

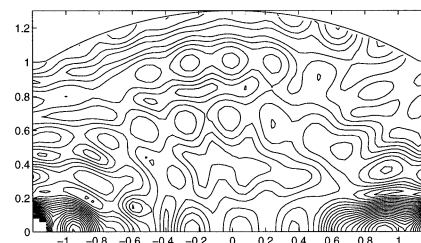
using an integral formulation at the extremities, like the “boundary element method” or the “infinite element method” (see Ref. 13).

The last frequency studied ($kR_0=15.7$) corresponds to five propagating modes in the straight portions with a sixth mode becoming propagating in the indentation. Apart from the increasing frequency, this case is also interesting because the sixth mode has a turning point and we wish to know if our method is able to deal with such a situation. Figure 19 shows the pattern of the modulus of the pressure compared to the FEM solution; the focalization has become more pronounced than with the two preceding frequencies. As in the previous case, incorrect termination conditions for the impedance have to be taken into account in order to get a very good agreement with the FEM code results.

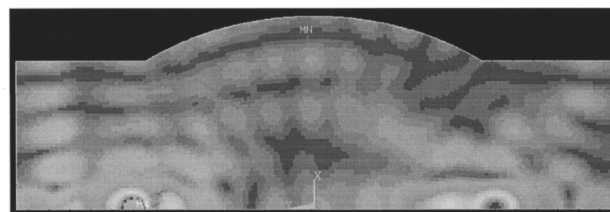
In Fig. 20, the modulus and phase profiles along the central line show excellent agreement with the FEM solution when the incorrect infinite termination condition is taken.



(a) multimodal



(b) multimodal, incorrect



(c) FEM code

FIG. 19. Modulus of the pressure, $kR_0=15.7$.

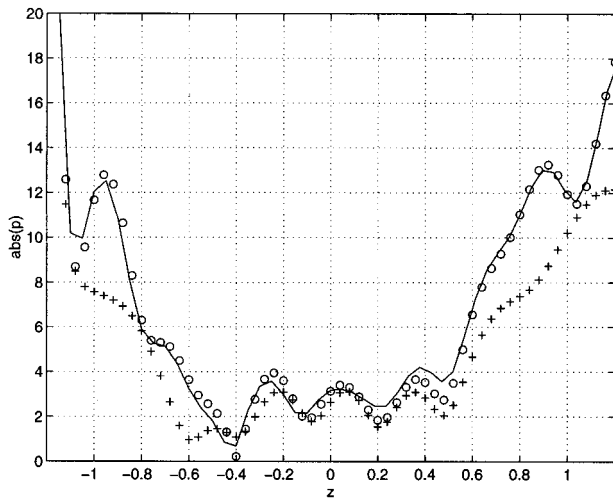
B. Reflection coefficient

Results for the reflection coefficient (defined in Part I) are studied in an ellipsoidal geometry where $L=10$ and $R_{\max}=1.1$ (geometry 1) or $R_{\max}=1.3$ (geometry 2). A common way to characterize a singularity in a waveguide, here the indentation, in a waveguide is to study the reflection coefficient as a function of the frequency.

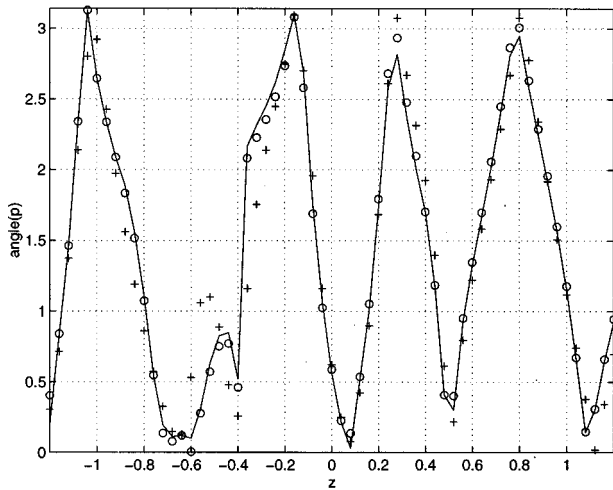
In this case, our method is especially convenient, since it is sufficient to calculate the impedance matrix from the left end to the beginning of the duct to get the reflection coefficient. We do not have to integrate the velocity or pressure equations. On the other hand, by using a FEM code, for instance, we would have to specify exact properties of the source, and the results obtained would have to be transformed to a suitable form to get the reflection coefficient.

In the two following examples, the boundary condition at the right of the indentation is taken as the characteristic matrix impedance, modeling the correct infinite termination. It has been assumed that a plane wave is incident at the left. By knowing the impedance at the left of the indentation, it is possible to obtain the energy reflection coefficient R which is defined as $R=W_r/W_i$, where W_r and W_i are, respectively, the reflected and incident energy flux.

Results for the two geometries considered are shown in Fig. 21. They display the behavior of R against f/f_{c1} where



(a) modulus of the pressure



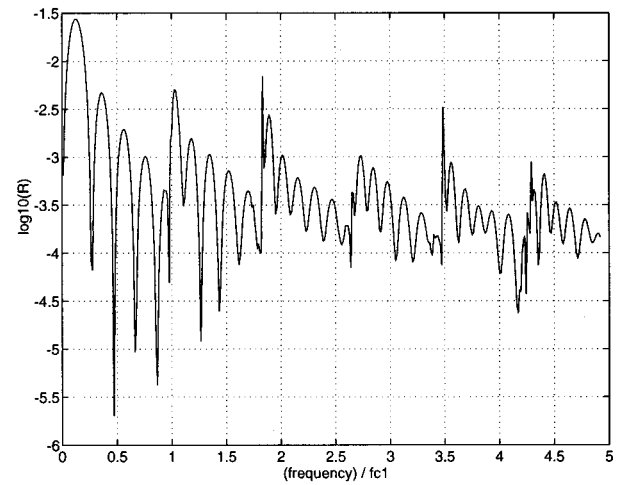
(b) phase of the pressure

FIG. 20. Modulus and phase of the pressure along the central line $r=0$, $kR_0=15.7$. (+): correct boundary condition; (O): incorrect boundary condition; plain line: FEM method.

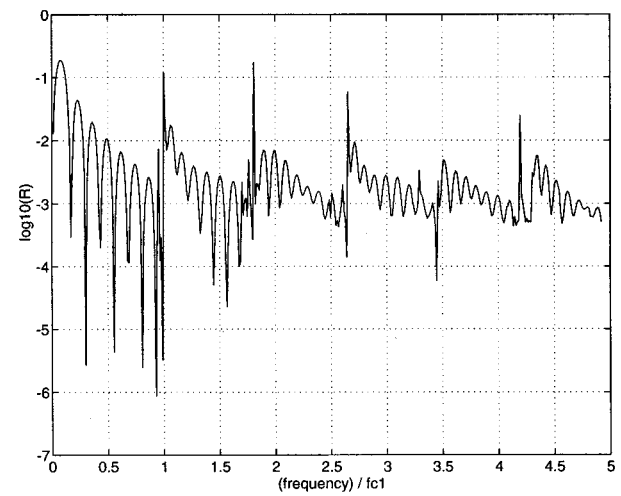
f is the frequency and $f_{c1}=(c\gamma_1)/(2\pi R_0)$ is the cutoff frequency of the first higher-order mode of the duct. The two geometries produce the same kind of results. The first major difference is the lower value of R in the geometry that has a lower radius R_{\max} in the indentation. It seems logical because R_{\max} measures the strength of the indentation. The second difference is in the number of oscillations between each cut-off frequency. This is due to the relation of these oscillations to the length of the indentations L_S ; $L_S=4.4$ for geometry one and $L_S=6.6$ for geometry two. In fact, $L_S=2\sqrt{L^2+4R_{\max}^2}\sqrt{1-1/R_{\max}^2}$.

Three principal features can be observed for the global behavior of the reflection coefficient.

First, the oscillations are due to quasiresonance of the elliptical indentation viewed as an open cavity. In an expansion chamber of length L_S they correspond to the condition $kL_S=n\pi$ under the plane-wave approximation. This condi-



(a) $R_{\max}=1.1$



(b) $R_{\max}=1.3$

FIG. 21. Reflection coefficient as a function of normalized frequency f/f_{c1} (f_{c1} : cutoff frequency of the first nonplane mode) for geometry 1 and 2.

tion expresses the transparency of the cavity since the impedance is then the same at the two extremities of the cavity. It yields five and eight oscillations for geometry 1 ($R_{\max}=1.1$) and geometry 2 ($R_{\max}=1.3$), respectively. From Fig. 21 it can be seen that it is roughly the number of oscillations we can observe.

Second, peaks correspond to each cutoff frequency. They can be understood by remarking that when $f=f_{cn}$ for some mode n , the n th component of the characteristic matrix goes to infinity. Then the end condition for this mode is equivalent to a wall condition and the reflection is enhanced.

Finally, the decrease of R between each cutoff frequency can be understood by drawing an analogy with a potential barrier in quantum mechanics; for the plane-wave approximation the equation for the pressure is

$$(Rp)'' + \left(k^2 - \frac{R''}{R}\right)(Rp) = 0,$$

and the indentation is equivalent to a potential $V(z) = R''/R$. So when the frequency increases, so does the energy k^2 , and the wave is more capable to overcome the potential V . This kind of analogy was developed by Benade and Jansson.¹⁴ Nevertheless, we notice that it is entirely valid if the junctions between the straight duct and the portion with varying cross section satisfy the continuity of both the function $R(z)$ and its first derivative $R'(z)$.¹⁵

IV. CONCLUSION

In this paper, we have shown how the multimodal method can be used to solve various problems concerning waveguides with varying cross section, with no restriction on the flare.

The convergence of the method has been investigated. The limit of the matched plane-wave approximation has been observed, and it appears that adding only a few modes, or even one mode in some cases, can be very effective in improving the accuracy of the modal approach.

The comparison with experiments for an baffled trombone shows better agreement than the plane-wave approximation, and we think that the remaining discrepancies could be due to the finite size of the baffle in the experiments. We plan to study this effect.

We also show that the multimodal method is able to deal with fairly high frequencies (five modes propagating) and to yield high-frequency results, like the focalization.

In conclusion, the multimodal method we have presented in Part I and Part II of this series of papers seems to be well adapted to the general form of waveguides with varying cross section in a large range of frequencies.

ACKNOWLEDGMENTS

One of the authors (V.P.) would like to thank the Gas Engineering Montrouge team of Schlumberger Industries for

scientific and part of financial supports. We also thank Nicolas Joly (CTTM) for interesting discussions on the trombone bell problem.

- ¹V. Pagneux, N. Amir, and J. Kergomard, "A study of wave propagation in varying cross-section waveguides by modal decomposition. Part I: Theory and validation," *J. Acoust. Soc. Am.* **100**, 2034–2048 (1996).
- ²V. Pagneux, J. Kergomard, and G. Marquette, *Propagation multimodale en géométrie complexe* (Congrès Français de Mécanique, Lille, 1993), pp. 1045–1049.
- ³J. Kergomard, "Une equation matricielle des pavillons acoustiques," *C. R. Acad. Sci. Paris Ser. II* **316**, 1691–1694 (1993).
- ⁴A. M. Bruneau, M. Bruneau, Ph. Herzog, and J. Kergomard, "Boundary layer attenuation of higher order modes in waveguides," *J. Sound Vib.* **119**, 15–27 (1987).
- ⁵W. E. Zorumski, "Generalized radiation impedances and reflection coefficients of circular and annular ducts," *J. Acoust. Soc. Am.* **54**, 1667–1673 (1972).
- ⁶Y. Kagawa, T. Yamabuchi, and T. Yoshikawa, "Finite element approach to acoustic transmission-radiation systems and application to horn and silencer design," *J. Acoust. Soc. Am.* **69**, 207–228 (1980).
- ⁷E. G. Williams, "Numerical evaluation of the radiation from unbaffled, finite plates using the FFT," *J. Acoust. Soc. Am.* **74**, 343–347 (1983).
- ⁸J. P. Dalmont and A. M. Bruneau, "Acoustic impedance measurement: plane-wave mode and first helical mode contributions," *J. Acoust. Soc. Am.* **91**, 3026–3033 (1992).
- ⁹N. Amir, G. Rosenhouse, and U. Shimoni, "Modal solution for the sound wave equation in spherical coordinates for non-canonical horns," *Acustica* **82**, 1–8 (1996).
- ¹⁰J. Kergomard, "Champ interne et champ externe des instruments à vent," Doctoral thesis, Université Paris 6 (1981).
- ¹¹P. Morse and U. Ingard, *Theoretical Acoustics* (McGraw-Hill, New York, 1968).
- ¹²P. E. Doak, "Excitation, transmission and radiation of sound from distribution source in hard-wall ducts of finite length," *J. Sound Vib.* **31**, 137–174 (1971).
- ¹³T. W. Dawson and J. A. Fawcett, "A boundary integral equation method for acoustic scattering matrix in a waveguide with nonplanar surface," *J. Acoust. Soc. Am.* **87**, 1110–1125 (1990).
- ¹⁴A. H. Benade and E. V. Jansson, "On plane wave and spherical waves in horns with nonuniform flare. Part I: Theory," *Acustica* **31**, 79–98 (1974).
- ¹⁵C. Depollier, J. Kergomard, and F. Laloe, "Localisation d'Anderson des ondes dans les réseaux acoustiques unidimensionnels aléatoires," *Ann. Phys.* **11**, 457–492 (1986).